

Dynamic vorticity banding in discontinuously shear thickening suspensions

R. N. Chacko,¹ R. Mari,² M. E. Cates,³ and S. M. Fielding¹

¹*Department of Physics, Durham University, Science Laboratories,
South Road, Durham DH1 3LE, United Kingdom*

²*Univ. Grenoble Alpes, CNRS, LIPhy, 38000 Grenoble, France*

³*DAMTP, Centre for Mathematical Sciences, University of Cambridge,
Wilberforce Road, Cambridge CB3 0WA, United Kingdom*

(Dated: August 16, 2018)

It has recently been argued that steady-state vorticity bands cannot arise in shear thickening suspensions, because the normal stress imbalance across the interface between the bands will set up particle migrations. In this Letter, we develop a simple continuum model that couples shear thickening to particle migration. We show by linear stability analysis that homogeneous flow is unstable towards vorticity banding, as expected, in the regime of negative constitutive slope. In full nonlinear computations, we show however that the resulting vorticity bands are unsteady, with spatiotemporal patterns governed by stress-concentration coupling. We furthermore show that these dynamical bands also arise in direct particle simulations, in good agreement with the continuum model.

Recent years have seen rapid advances in understanding the rheology of dense non-Brownian suspensions, comprising solid particles in a Newtonian fluid at volume fraction ϕ close to isotropic jamming. In particular, the phenomenon of shear thickening [1, 2], in which the viscosity increases with shear stress σ , has recently been understood as an evolution from lubricated to frictional particle interactions, as the hydrodynamic forces that push particles together overcome short-ranged repulsive forces keeping them apart [3–16]. When strong, this effect creates, for states of homogeneous shear rate $\dot{\gamma}$, a constitutive curve $\sigma(\dot{\gamma})$ that is S-shaped [17, 18]: a positively sloping hydrodynamic branch of low viscosity at low stresses connects to a positively sloping frictional branch of high viscosity at high stresses via a negatively sloped region at intermediate stresses. A slowly increasing imposed shear rate then provokes a discontinuous jump, between the low and high viscosity branches, in the measured or ‘macroscopic’ flow curve. This is known as discontinuous shear thickening (DST) [1, 2].

At imposed macroscopic shear stress, when $d\sigma/d\dot{\gamma} < 0$ one expects homogeneous steady flow to be unstable, at least for large system sizes [19]. (For the system sizes used in particle-based simulations, this expectation is not always met [18].) Consistent with this expectation, an S-shaped constitutive curve as described above admits (in principle) steady states comprising layers of material coexisting at a common shear rate but with different shear stresses. These are force-balanced so long as they stack with normals in the vorticity direction, and are then known as “vorticity bands” [20]. In dense suspensions, however, steady state vorticity bands are argued to be ruled out by the differences in normal stress that generally arise across the interface between bands, leading to a particle migration flux [21]. Suggestively, experiments on suspensions and a modelling and simulation study on the related system of dry frictional grains have

revealed an unsteady strain rate signal under conditions of constant imposed macroscopic shear stress in the DST regime, with complicated time dependence [21–24].

In this Letter, we advance the understanding of dynamic vorticity banding in dense suspensions. First, we propose a scalar continuum constitutive model for the relevant rheology, by combining the Wyart-Cates theory [17] (which captures shear thickening but assumes homogeneous flow) with a suspension balance model of particle migration [25–29]. Second, for this model we use linear stability analysis to determine when a homogeneous shear flow is unstable to fluctuations along the vorticity axis, finding instability whenever $d\sigma/d\dot{\gamma} < 0$ in the limit of large system size. Third, we elucidate numerically the model’s full nonlinear vorticity-banding dynamics, identifying two distinct spatio-temporal patterns that we shall term “travelling bands” (TB) and “locally oscillating bands” (LOB). The LOB state shows an oscillating bulk shear rate signal, as seen experimentally [21, 23]. Finally, we perform particle-based simulations using the so-called Critical Load Model [18] and show that this also has TB and (at least transiently) LOB states, in close counterpart to the continuum model.

We consider Stokes flow of a dense suspension sheared between hard flat plates at $y = 0, L_y$ under conditions of constant imposed shear stress. This produces a velocity field $\bar{\mathbf{v}}(y) = (\dot{\gamma}(t)y, 0, 0)$ with a shear rate $\dot{\gamma}(t)$ that is in general time-dependent. (Here $\bar{\mathbf{v}}$ denotes the suspension velocity averaged over the particle and solvent components introduced below.) The velocity is along the x direction, its gradient along y , and the vorticity direction is z . (See [30] for a diagram.) As appropriate to describe vorticity banding, we assume spatial invariance in the flow direction x and flow-gradient direction y , allowing spatial variations only along z . There can be no such variation for the shear rate $\dot{\gamma}(t)$ which follows the relative speed of the plates. The dynamical variables

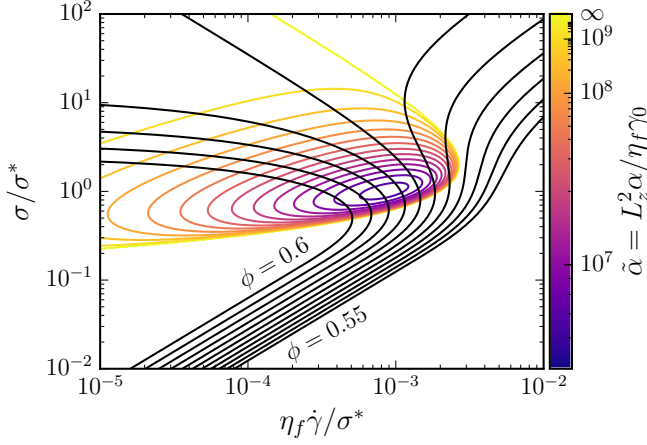


FIG. 1. Nondimensionalized homogeneous constitutive curves (black lines) for volume fractions $\phi \in [0.55, 0.6]$, and stability boundaries (coloured lines) enclosing the region of unstable homogeneous flow for several $\tilde{\alpha} \in [5 \times 10^6, \infty]$, for $\tilde{\alpha}^{-1/2}$ values linearly spaced. A given value of $\tilde{\alpha}^{-1/2}$ corresponds to a given value of the inverse system size a/L_z , for fixed bulk rheology parameters η_f and γ_0 .

that we consider are therefore the component $\sigma_{zz}(z, t)$ of the particle phase stress tensor (whose behavior is similar to that of $\sigma_{xy}(z, t)$ [17]), the fraction of frictional contacts $f(z, t)$, which is the microstructural order parameter entering the Wyart-Cates theory [17], and the volume fraction $\phi(z, t)$. Note that the zz component of stress is actually negative in dense suspensions [1], but we work throughout with its absolute value and denote this simply by σ_{zz} .

The Wyart-Cates theory [17] gives a scalar constitutive model for the steady state homogeneous shear rheology of dense suspensions. While initially presented as a model for the shear stress σ_{xy} , this equally describes σ_{zz} , because all stress components evolve in a similar way near jamming [35] and across DST [9]. The associated viscosity is taken to diverge as the volume fraction ϕ approaches a critical jamming point ϕ_J :

$$\eta(\phi, \phi_J) \equiv \sigma_{zz}/\dot{\gamma} = \eta_0(\phi_J - \phi)^{-\nu}, \quad (1)$$

where η_0 is, within the range of ϕ of interest here, of order the solvent viscosity η_f and effectively constant, so hereafter we set $\eta_0 = \eta_f$ for simplicity; ν is likewise a constant. Shear thickening is then captured by assuming that at low stresses repulsive forces maintain a lubrication film between particles, with a fraction of frictional contacts $f \approx 0$, whereas at high stresses frictional contacts dominate the rheology, $f \approx 1$. The critical volume fraction for jamming depends smoothly on stress, varying linearly with f to connect the critical value ϕ_J^0 for frictionless jamming at low stresses to the one for frictional particles $\phi_J^\mu < \phi_J^0$ at large stresses:

$$\phi_J(f) = \phi_J^0 - f(\phi_J^0 - \phi_J^\mu). \quad (2)$$

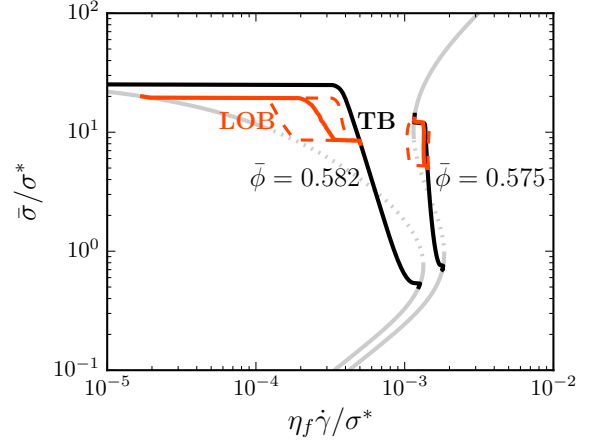


FIG. 2. Macroscopic flow curves for $\alpha = 10^9$ with $\bar{\phi} = 0.575$ and $\bar{\phi} = 0.582$, obtained by sweeping stress up and down from a TB state (black lines) and from a LOB state (red lines). For LOB, solid lines are the time-averaged flow curves, while dashed lines are the low and high limits of shear rate oscillations. The underlying homogeneous steady state flow curves (grey lines) show domains of linear stability (solid lines) and instability (dashed lines).

Here μ is the particle friction coefficient.

For the dependence of the fraction of frictional contacts f on stress σ_{zz} , particle simulations suggest a relation

$$f^{\text{ss}}(\sigma_{zz}) = \exp(-\sigma^*/\sigma_{zz}) \quad (3)$$

in steady state, where $\sigma^* = CF^*/a^2$. This depends on the typical repulsive force F^* that must be overcome to create a contact and the typical particle radius a ; particle simulations suggest $C \approx 1.45$ [9, 36]. Departing now from the steady-state assumptions of [17], we assume that f does not react infinitely fast to changes in stress [18, 37], following instead

$$\partial_t f = -\frac{\dot{\gamma}}{\gamma_0} [f - f^{\text{ss}}]. \quad (4)$$

Note that this evolution involves a characteristic strain scale γ_0 , of order the strain required to evolve from one steady-state to another (for instance on flow reversal [38]). For the typical volume fractions considered here, particle simulations suggest $\gamma_0 = O(10^{-2})$ [18].

Next we assume that particle migration between vorticity bands is driven by the difference in normal stress σ_{zz} that will in general exist across the interface between them. We model this via a “two-fluid” [39] or “suspension balance” model [25–29]. The divergence of the particle stress gives a force imbalance on the particle phase, which must be rebalanced by a drag between the particles (p) and fluid (f) due to an interphase relative velocity $v_z^p - v_z^f = v_z^p/(1 - \phi)$, found using $\bar{v}_z = \phi v_z^p + (1 - \phi)v_z^f$. The resulting balance condition, $\partial_z \sigma_{zz} = -\phi \alpha v_z^p$, involving an interphase drag parameter α , then implies that particles migrate from regions of high to low stress.

Conservation of mass now imposes $\partial_t \phi + \partial_z(v_z^p \phi) = 0$, which gives

$$\partial_t \phi = -\frac{1}{\alpha} \partial_z^2 \sigma_{zz}. \quad (5)$$

Particle simulations [40] suggest the drag coefficient α ranges from $4.5\eta_f a^{-2}$ for $\phi \rightarrow 0$ to $225\eta_f a^{-2}$ for $\phi = 0.64$. However, in this work, variations in ϕ will be 5% or less, so we treat α as a ϕ -independent model parameter.

Eqs. 1–5 define our model. It contains the parameters $\eta_f, \nu, \phi_J^\mu, \phi_J^0, \sigma^*, \gamma_0$ and α , along with the cell length in the vorticity direction L_z , the global volume fraction $\bar{\phi} = L_z^{-1} \int_0^{L_z} dz \phi$, and the global mean particle stress $\bar{\sigma} = L_z^{-1} \int_0^{L_z} dz \sigma_{zz}$ as imposed at the walls. We choose L_z as the length unit, σ^* as the stress unit, and η_f/σ^* as the time unit. Except when explicitly comparing with the simulation data, we also choose to rescale all strains by γ_0 , so setting $\gamma_0 = 1$. We set rheological parameters compatible with the ones of spherical particles with moderate polydispersity, setting $\nu = 2.0$ [35, 36], $\phi_J^\mu = 0.58$ (for friction $\mu \approx 1$ [9, 35]) and $\phi_J^0 = 0.64$ [41, 42]. There then remain just three dimensionless parameters: a rescaled drag $\tilde{\alpha} = L_z^2 \alpha / \eta_f \gamma_0$ (effectively a measure of the system size L_z/a), rescaled stress $\tilde{\sigma} = \bar{\sigma}/\sigma^*$ and volume fraction $\bar{\phi}$. We drop tildes and denote these $\alpha, \bar{\sigma}$ and $\bar{\phi}$ hereafter.

The overbars are in turn dropped when discussing strictly homogeneous, unbanded steady states, as described by the constitutive curves $\sigma(\dot{\gamma})$. These are just the stationary solutions of Eqs. 1–4, and coincide directly with those of [17]. They are shown as black lines in Fig. 1. At low volume fraction $\phi < \phi_{\text{DST}}$, they are monotonic. For $\phi_{\text{DST}} < \phi < \phi_J^\mu$ they are S-shaped, with a regime in which $d\sigma/d\dot{\gamma} < 0$, giving discontinuous shear thickening. At even larger $\phi > \phi_J^\mu$, they bend right back to ascend the axis $\dot{\gamma} = 0$ above a ϕ -dependent shear jamming stress σ_J , with flow only possible for stresses $\sigma < \sigma_J$.

For any initial state on such a constitutive curve, the volume fraction ϕ and fraction of frictional contacts f are defined to be uniform. We now perform a linear stability analysis to determine whether any such “base state” is stable, by adding to it small-amplitude perturbations $\propto e^{ikz}$ in both f and ϕ . Expanding Eqs. 1–5 to first order in the corresponding amplitudes we find linear instability [43]

$$\left[\frac{d\sigma}{d\dot{\gamma}} \right]^{-1} < -\frac{k^2}{\alpha} \frac{1}{\eta} \frac{\partial \eta}{\partial \phi}. \quad (6)$$

In regimes of high σ or low ϕ , we also find an oscillatory component to the growing perturbations. For an infinitely large system, that is, $\alpha \rightarrow \infty$, this yields the familiar mechanical instability criterion for vorticity banding, $d\sigma/d\dot{\gamma} < 0$. When the system size is finite, the unstable region shrinks, with stability boundaries shown as colored lines in Fig. 1.

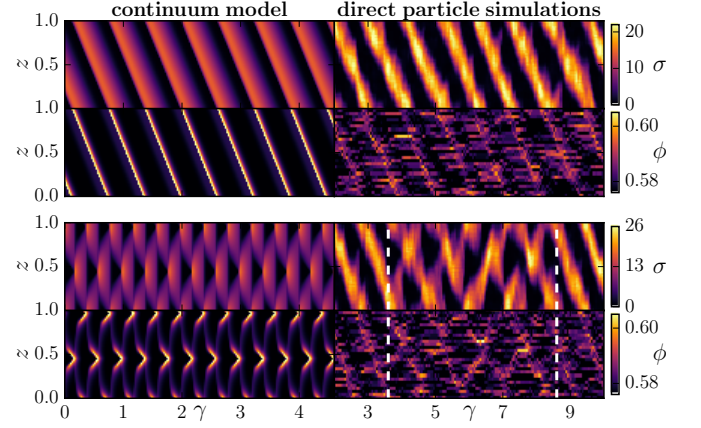


FIG. 3. Comparison of volume fraction and stress space-strain plots between long-time inhomogeneous flows in the (left) continuum model and (right) direct particle simulations at a volume fraction $\bar{\phi} = 0.58$. The parameters for the continuum model are $\gamma_0 = 0.023$ and $\alpha = 1.3 \times 10^8$, while the particle simulation use $L_z/a = 815$ and we measure $\gamma_0 = 0.023$ [18] and $\alpha = (1.4 \pm 0.3) \times 10^8$. TB solutions at an imposed stress $\bar{\sigma} = 6.525$ (top) and LOB solutions at $\bar{\sigma} = 7.25$ (bottom). (All stresses are nondimensionalized by setting $\sigma^* = 1$.) LOB are only visible transiently in the simulations. Note the different scales for the strain in the continuum model and the particle simulations: the model predicts bands moving roughly twice faster than in the simulations.

The mechanism of this instability is as follows. Temporarily ignoring variations in ϕ , Eqs. 1–4 effectively reduce to (a) $\dot{\gamma} = \sigma/\eta(f)$ and (b) $\dot{f} = -[f - f^{\text{SS}}(\sigma)]$. Recalling that $\dot{\gamma}$ must remain uniform in z while σ and f can vary, we imagine a localised fluctuation in which σ slightly increases at some z : (b) then requires that f correspondingly also increases. For large enough $d\eta/df > 0$, σ must increase even further to maintain uniform $\dot{\gamma}$ along z via (a). This gives positive feedback and instability, irrespective of wave vector k . We now relax the assumption of constant ϕ , noting that the ϕ relaxation depends on k , and is always stabilizing: whenever σ increases locally, there is an outward migration of particles, thereby locally decreasing ϕ and hence the viscosity. The competition between these processes restricts the unstable f dynamics to large length scales, because the time for particle migration increases with distance.

Having shown a state of initially homogeneous flow to be linearly unstable if Eq. (6) is satisfied, we now numerically integrate the model equations to elucidate the full nonlinear dynamics that prevails at long times. We do so for a representative value of $\alpha = 10^9$ and for two volume fractions: $\bar{\phi} = 0.575$, for which the constitutive curve is S-shaped; and $\bar{\phi} = 0.582$, for which it folds right back to the $\dot{\gamma} = 0$ axis. Taking as our initial condition a state of homogeneous shear on the constitutive curve for some imposed $\bar{\sigma}$, subject to small-amplitude perturbations, we find one of two possible competing long-time

states of dynamical vorticity bands: a locally oscillating band (LOB) state for imposed shear stresses in the vicinity of $\bar{\sigma} = 10$, and a travelling band (TB) state otherwise. Starting from the LOB (resp. TB) state, we then quasi-statically sweep $\bar{\sigma}$ up and (in a separate run) down from these values, generating the red (resp. black) macroscopic flow curves shown in Fig. 2 (see [30] for details).

A TB state, pertaining to the black flow curve, is shown in Fig. 3 (top left). Here the steady-state bulk shear rate $\dot{\gamma}(t) = \text{const.}$, and localised pulses travel along the vorticity axis at constant speed in one direction. (The direction represents a spontaneously broken symmetry, depending sensitively on the initial noise.) An LOB state, pertaining to the red flow curve, is shown in Fig. 3 (bottom left). Here the bulk shear rate at constant imposed stress shows sustained oscillations in time, reminiscent of experimental observations [21, 23]. In Fig. 2, the average of the oscillation is shown by the solid red line, and the limits by the dotted red lines. These states lie within the region of oscillatory linear instability; spatiotemporally they exhibit locally oscillating bands comprising two excitations that travel in opposite directions and intermittently collide. Such collisions coincide with a drop in the oscillating bulk shear rate signal. For the higher volume fraction, $\bar{\phi} = 0.582$, homogeneous flow is recovered above some stress threshold $\sigma = \sigma^{\text{hom}} < \sigma_J$; but flow then arrests completely at $\sigma \geq \sigma_J$, where the underlying constitutive curve re-joins the vertical axis [44].

We now compare these continuum results to direct particle simulations. These use 8000 bidisperse spheres (radii a and $1.4a$ in equal volume proportions), sheared under constant global shear stress $\bar{\sigma}_{xy}$ in a tri-periodic box of size $L_x = L_y = 10.2a$ and $L_z = 815a$ to allow for fully developed vorticity bands [30], using Lees-Edwards boundary conditions [45]. (Note that $\bar{\sigma}_{zz}$ was controlled in the continuum model; this should not matter as previously discussed.) The spheres interact through both lubrication and contact forces [9], with any contact force becoming frictional (with friction coefficient $\mu = 1$) once the normal part exceeds a fixed value F^* [30]. This “Critical Load Model” captures both DST and jamming, but previous work [9] used much smaller L_z values, precluding the vorticity instabilities addressed here. With $\mu = 1$, the values of ν , ϕ_J^μ and ϕ_J^0 are consistent with the ones we set for the continuum model, giving a good agreement for the homogeneous steady state flow curves [36].

In our large- L_z simulations, we indeed find dynamic vorticity banding, with two distinct dynamical states, in close analogy with those of our continuum model. As seen in the top right of Fig. 3, we recover the TB solutions at lower stresses. We find good qualitative agreement between simulations and our continuum model (top left of Fig. 3) in the overall dynamics of stress and volume fraction fields. To perform the comparison, we used model parameters $\gamma_0 = 0.023$ and $\alpha = 1.3 \times 10^8$, based on their

measured value in the simulations [46]. Both continuum model and particle simulations show slight accumulation of particles at the front of the travelling thickened band, albeit with somewhat flatter stress profiles in the simulations than in the model (not shown). The continuum model’s prediction for the speed of the TB is in good qualitative agreement with our particle simulations, but roughly a factor 2 larger. At higher stresses, our simulations also exhibit the LOB states of the continuum model, but we have so far only found these as a transient effect in the particle simulations, with LOB always eventually giving way to TB: see the lower panel of Fig. 3.

In summary, we have proposed a continuum model for the vorticity instabilities of a shear-thickening suspension held at a constant macroscopic stress in the unstable part of the constitutive curve where $d\sigma/d\dot{\gamma} < 0$. Its predictions compare very well with our particle based simulations, including a regime of oscillating macroscopic shear rates as found experimentally [21, 23]. Crucially, the unsteady behavior results from a bulk rheological mechanism, not from coupling with the mechanical response of the rheometer, even if the latter plays a part in some experiments [23]. Particle migration is crucial: the banding dynamics relies on small concentration variations that have large rheological effects close to jamming, as reported previously for colloidal glasses in pipe flow [47].

Observing the predicted spatiotemporal bands directly in experiments, by measuring local stress fields and small concentration fluctuations, may prove challenging. The velocity field along the vorticity direction also bears a signature of the bands due to particle migration, which could be more accessible. Very recent experiments do report vorticity bands in cornstarch suspensions under controlled stress, similar to those presented here in shape, size and velocity [48]. However, the banding signature involves the flow (v_x) velocity component; this may stem from differential wall slip induced by a frictional band moving along the vorticity direction.

While we focused here on a constitutive model involving only the normal stress along the vorticity direction, the physical ingredients in our model may also admit instabilities along the gradient and/or flow directions. Without volume fraction variations, however, homogeneous shear flow is predicted to be stable against gradient perturbations in the absence of inertia [18], for constitutive curves of the shapes considered here. Any instability in the gradient direction would therefore have to be driven by particle migration (and/or inertial) effects, and is likely to be subdominant to the vorticity banding considered here. Indeed some experiments in the discontinuous shear thickening regime report a flowing gradient band of lower concentration coexisting with a densely jammed band [49]. For very large systems, inertia will separately trigger gradient instabilities [4, 50]. Our coupled model of shear thickening and particle migration represents a first step towards explaining the full

range of unsteady flows close to the jamming transition in dense suspensions and, we hope, will stimulate systematic experimental studies of this regime.

We thank M. Hermes, I. Peters, B. Saint-Michel, T. Gibaud and S. Manneville for insightful discussions. Work funded in part by SOFI CDT, Durham University, and EPSRC (EP/L015536/1); the European Research Council under the European Union's Seventh Framework Programme (FP7/2007-2013) and Horizon 2020 Programme / ERC grant agreements 279365 and 740269. MEC is funded by the Royal Society.

-
- [1] J. Mewis and N. J. Wagner, *Colloidal Suspension Rheology* (Cambridge University Press, Cambridge, England, 2011).
 - [2] E. Brown and H. M. Jaeger, Rep. Prog. Phys. **77**, 046602 (2014).
 - [3] D. Lootens, H. van Damme, Y. Hémar, and P. Hébraud, Phys. Rev. Lett. **95**, 268302 (2005).
 - [4] I. A. Bashkirtseva, A. Y. Zubarev, L. Y. Isakova, and L. B. Ryashko, Colloid J. **71**, 446 (2009).
 - [5] E. . Brown and H. M. Jaeger, J. Rheol. **56**, 875 (2012).
 - [6] N. Fernandez, R. Mani, D. Rinaldi, D. Kadau, M. Mosquet, H. Lombois-Burger, J. Cayer-Barrioz, H. J. Herrmann, N. D. Spencer, and L. Isa, Phys. Rev. Lett. **111**, 108301 (2013).
 - [7] R. Seto, R. Mari, J. F. Morris, and M. M. Denn, Phys. Rev. Lett. **111**, 218301 (2013).
 - [8] C. Heussinger, Phys. Rev. E **88**, 050201 (2013).
 - [9] R. Mari, R. Seto, J. F. Morris, and M. M. Denn, J. Rheol. **58**, 1693 (2014).
 - [10] R. Mari, R. Seto, J. F. Morris, and M. M. Denn, Proc. Natl. Acad. Sci. U.S.A. **112**, 15326 (2015).
 - [11] N. Y. C. Lin, B. M. Guy, M. Hermes, C. Ness, J. Sun, W. C. K. Poon, and I. Cohen, Phys. Rev. Lett. **115**, 228304 (2015).
 - [12] B. M. Guy, M. Hermes, and W. C. K. Poon, Phys. Rev. Lett. **115**, 088304 (2015).
 - [13] J. Comtet, G. Chatté, A. Niguès, L. Bocquet, A. Siria, and A. Colin, Nat. Commun. **8**, 15633 (2017).
 - [14] C. Clavaud, A. Bérut, B. Metzger, and Y. Forterre, Proc. Natl. Acad. Sci. U.S.A. **114**, 5147 (2017).
 - [15] L. C. Hsiao, S. Jamali, E. Glynos, P. F. Green, R. G. Larson, and M. J. Solomon, Phys. Rev. Lett. **119**, 158001 (2017).
 - [16] C.-P. Hsu, S. N. Ramakrishna, M. Zanini, N. D. Spencer, and L. Isa, Proc. Natl. Acad. Sci. U.S.A. **115**, 5117 (2018).
 - [17] M. Wyart and M. E. Cates, Phys. Rev. Lett. **112**, 098302 (2014).
 - [18] R. Mari, R. Seto, J. F. Morris, and M. M. Denn, Phys. Rev. E **91**, 052302 (2015).
 - [19] J. Yerushalmi, S. Katz, and R. Shinnar, Chem. Eng. Sci. **25**, 1891 (1970).
 - [20] P. D. Olmsted, Rheol. Acta **47**, 283 (2008).
 - [21] M. Hermes, B. M. Guy, W. C. K. Poon, G. Poy, M. E. Cates, and M. Wyart, J. Rheol. **60**, 905 (2016).
 - [22] M. Neuville, G. Bossis, J. Persello, O. Volkova, P. Boustingorry, and M. Mosquet, J. Rheol. **56**, 435 (2012).
 - [23] G. Bossis, P. Boustingorry, Y. Grasselli, A. Meunier, R. Morini, A. Zubarev, and O. Volkova, Rheol. Acta **56**, 415 (2017).
 - [24] M. Grob, A. Zippelius, C. Heussinger, Phys. Rev. E **93**, 030901(R) (2016).
 - [25] P. R. Nott and J. F. Brady, J. Fluid Mech. **275**, 157 (1994).
 - [26] J. F. Morris and F. Boulay, J. Rheol. **43**, 1213 (1999).
 - [27] Y. Yurkovetsky and J. F. Morris, J. Rheol. **52**, 141 (2008).
 - [28] D. Lhuillier, Phys. Fluids **21**, 023302 (2009).
 - [29] P. R. Nott, E. Guazzelli, and O. Pouliquen, Phys. Fluids **23**, 043304 (2011).
 - [30] See Supplemental Material [url] for additional detail on our methodologies, which includes Refs. [31–34].
 - [31] W. H. Press, S. A. Teukolsky, W. T. Vetterling, and B. P. Flannery, *Numerical Recipes*, 3rd ed. (Cambridge University Press, New York, USA, 2007).
 - [32] D. J. Jeffrey and Y. Onishi, Journal of Fluid Mechanics **139**, 261 (1984).
 - [33] M. Trulsson, B. Andreotti, and P. Claudin, Physical Review Letters **109**, 118305 (2012).
 - [34] D. J. Jeffrey, Physics of Fluids A: Fluid Dynamics (1989-1993) **4**, 16 (1992).
 - [35] F. Boyer, É. Guazzelli, and O. Pouliquen, Phys. Rev. Lett. **107**, 188301 (2011).
 - [36] A. Singh, R. Mari, M. M. Denn, and J. F. Morris, J. Rheol. **62**, 457 (2018).
 - [37] E. Han, M. Wyart, I. R. Peters, and H. M. Jaeger, Phys. Rev. Fluids **3**, 073301 (2018).
 - [38] R. N. Chacko, R. Mari, S. M. Fielding, and M. E. Cates, Journal of Fluid Mechanics **847**, 700 (2018).
 - [39] M. Doi, *Soft Matter Physics* (Oxford University Press, Oxford, England, 2013).
 - [40] M. A. van der Hoef, R. Beetstra, and J. A. M. Kuipers, J. Fluid Mech. **528**, 233 (2005).
 - [41] G. D. Scott, Nature **188**, 908 (1960).
 - [42] J. G. Berryman, Phys. Rev. A **27**, 1053 (1983).
 - [43] Linear instability arises for positive real part $\Re \omega > 0$ for the eigenvalue ω of the linearized dynamics. An oscillatory component arises for non-zero imaginary part $|\Im \omega| > 0$.
 - [44] We note that the composite (macroscopic) flow curves are tilted – as opposed to vertical, as would have been expected without concentration coupling [20] – and that negatively sloping macroscopic flow curves were seen experimentally in [51].
 - [45] A. W. Lees and S. F. Edwards, J. Phys. C **5**, 1921 (1972).
 - [46] Specifically, we take γ_0 from [18], and take $\alpha = (1.4 \pm 0.3) \times 10^8$ from fits to the measured relation between the particle phase velocity and stress gradient $\partial_z \sigma_{zz} = -\phi \alpha v_z^p$.
 - [47] R. Besseling, L. Isa, P. Ballesta, G. Petekidis, M. E. Cates, and W. C. K. Poon, Phys. Rev. Lett. **105**, 268301 (2010).
 - [48] B. Saint-Michel, T. Gibaud, and S. Manneville, Phys. Rev. X **8**, 031006 (2018).
 - [49] A. Fall, F. Bertrand, D. Hautemayou, C. Mezière, P. Moucheront, A. Lemaître, and G. Ovarlez, Phys. Rev. Lett. **114**, 098301 (2015).
 - [50] H. Nakanishi, S.-I. Nagahiro, and N. Mitarai, Phys. Rev. E **85**, 011401 (2012).

- [51] Z. Pan, H. de Cagny, B. Weber, and D. Bonn, Phys. Rev. E **92**, 032202 (2015).